3D periodic polyimide nano-networks for ultrahigh-rate and sustainable energy storage

Journal:	*Energy & Environmental Science*
Manuscript ID	EE-ART-06-2021-001739.R1
Article Type:	Paper
Date Submitted by the Author:	02-Aug-2021
Complete List of Authors:	Ham, Youngjin; Korea Advanced Institute of Science and Technology, Department of Materials Science and Engineering Fritz, Nathan; University of Illinois at Urbana-Champaign, Department of Materials Science and Engineering Hyun, Gayea; Korea Advanced Institute of Science and Technology, Department of Materials Science and Engineering Lee, Young Bum; University of Illinois at Urbana-Champaign, Department of Materials Science and Engineering Nam, Jong Seok; Korea Advanced Institute of Science and Technology, Department of Materials Science and Engineering Kim, Il-Doo; Korea Advanced Institute of Science and Technology, Department of Materials Science and Engineering Braun, Paul; University of Illinois at Urbana-Champaign, Department of Materials Science and Engineering Jeon, Seokwoo; Korea Advanced Institute of Science and Technology, Department of Materials Science and Engineering

ARTICLE

3D periodic polyimide nano-networks for ultrahigh-rate and sustainable energy storage

Received 00th January 20xx,
Accepted 00th January 20xx

DOI: 10.1039/x0xx00000x

Youngjin Ham,[a] Nathan J. Fritz,[b] Gayea Hyun,[a] Young Bum Lee,[b] Jong Seok Nam,[a] Il-Doo Kim,*[a] Paul V. Braun,*[bc] and Seokwoo Jeon*[ad]

Organic molecules with redox-active motifs are of great interest for next-generation electrodes for sustainable energy storage. While there has been significant progress in designing redox-active molecules, the practical requirements of high electrochemical activity and stability, as well as rapid kinetics for fast charging, are motivating a search for methods to engineer three-dimensional (3D) structures of organic-based electrodes. Here, we demonstrate a lithographic fabrication strategy for realizing a 3D bicontinuous nano-network consisting of a periodically porous nickel-supported redox-active polyimide layer (pore radius <300 nm), which provides highly conductive pathways for electron and ion transport. Through super-lithiation of nearly all unsaturated C=C bonds in this 3D-structured anode, a high reversible capacity of 1260 mAh g^{-1} and 82.8% capacity retention over 250 cycles at 10C rate are realized. Rates up to 400C for lithium-ion storage of organic anode are achieved for the first time, opening up new engineering opportunities for high-performance organic batteries.

Broader context

Rising concerns on the imminent environmental crisis have motivated a search for green technologies such as electric vehicles. Lithium-ion batteries (LIBs) are the most widely adopted energy storage systems for current electric vehicles due to their low self-discharge rate (<5% of the capacity per month). However, conventional electrodes for LIBs are based on metals, which bring us sustainability challenges of resources, cost, and environmental issues. Furthermore, breakthroughs in the development of inorganic-based electrodes to further improve the energy density are believed to reach their limitations. Considering these economic, environmental, and technological perspectives, lightweight and renewable organic materials are seeing a surge in popularity as attractive candidates for next-generation electrodes. In this work, we focus on revolutionizing rechargeable organic batteries with three-dimensional (3D) periodic nano-network anodes, consisting of submicron-porous Ni embedded inside a multi-electron redox-active polyimide layer. We unveil the effect of engineering organic nano-networks on superior charge transfer kinetics and the reaction chemistry exploiting promoted super-lithiation in this architecture. Our 3D anodes with incomparably high-rate cycling stability overcome the limitations in conventional anodes such as low capacities of graphite and volume expansion issue in silicon, raising new feasibility for widespread application of organic electrodes in practical battery systems.

Introduction

Growing demand for sustainable energy storage solutions for electric vehicles and portable electronics has driven interest in naturally abundant organic materials containing redox centers.[1–3] Redox-active organic materials offer inherent advantages of lightness, high theoretical capacity, low environmental footprint, and molecular tunability not provided by conventional inorganic anode (e.g., graphite, alloys, and metal oxides) and cathode (e.g., $LiNi_{0.5}Mn_{1.5}O_4$) materials found in current lithium-ion batteries (LIBs).[4] However, the practical application of organic electrodes remains challenging. Major issues of organic electrodes include poor cycling performance originating from the high solubility of most organics in common electrolytes and their inferior rate capability due to intrinsically low electrical conductivities of most organics. Recent reports described strategies to overcome the aforementioned challenges include molecular-level designs to alleviate dissolution into the electrolyte by polymerizing small redox-active molecules or optimizing molecular skeletons.[5,6] Other strategies are integrating organic molecules with a conductive matrix into structured electrodes.[7] Most of the significant

---

[a] *Department of Materials Science and Engineering, Korea Advanced Institute of Science and Technology (KAIST), 291 Daehak-ro, Yuseong-gu, Daejeon 34141, Republic of Korea. E-mail: jeon39@kaist.ac.kr, idkim@kaist.ac.kr*

[b] *Department of Materials Science and Engineering, University of Illinois Urbana-Champaign, Urbana, Illinois 61801, USA. E-mail: pbraun@illinois.edu*

[c] *Materials Research Laboratory and Beckman Institute for Advanced Science and Technology, University of Illinois Urbana-Champaign, Urbana, Illinois 61801, USA.*

[d] *Advanced Battery Center, KAIST Institute for the NanoCentury, 291 Daehak-ro, Yuseong-gu, Daejeon 34141, Republic of Korea.*

† Electronic Supplementary Information (ESI) available. See DOI: 10.1039/x0xx00000x

progress to-date has been related to the development of organic cathodes rather than anodes.[4,8] Much less emphasis has been placed on high-performance organic anodes because their redox potentials are usually in the range of 1.5 to 4.0 V versus Li/Li$^+$, which is too high to provide high energy density LIBs.[8]

Recently, conjugated carbonyl compounds based on multiple ring systems have received attention as low voltage (<3.0 V) organic anodes.[9,10] In large conjugated systems containing C_6 aromatic rings, an interesting super-lithiation phenomenon of unsaturated C=C bonds of each ring governs the redox reaction which forms the Li_6/C_6 complex,[11–13] with unexpected theoretical capacities up to 2000 mAh g^{-1}. Despite recent efforts to explore new conjugated carbonyl materials exploiting super-lithiation, their electrically insulating properties not only lead to unsatisfactory rate capability (typically less than 500 mAh g^{-1} at 3C rate) but also limit the full-utilization of their electrochemical activity, resulting in capacities far below theoretical values. Traditional approaches of adding standard conducting agents (e.g., Super-P)[10,12] or by applying these materials on carbon-based conductive matrixes (e.g., carbon nanotubes[9,11] and random porous carbon foam[13]), which yield structures with inhomogeneous electrical conductivities, are undesirable for promoting super-lithiation of internal active sites of these compounds. It is our hypothesis that realization of super-lithiation of conjugated carbonyl anodes requires a strategy which enables efficient electron conduction and facile ion transport.

Here, we demonstrate a three-dimensional (3D) bicontinuous nano-network architecture consisting of a periodic, porous Ni support embedded inside a multi-redox organic layer to overcome the challenges outlined above. Highly ordered, submicron-porous 3D Ni nanostructure is prepared by proximity-field nanopatterning (PnP), a highly reproducible and scalable optical lithographic technique.[14–20] Through structural engineering of Ni, which possesses exceptional hardness, electrochemical stability, and high electrical conductivity (1.43×10^7 S m^{-1}), the 3D Ni provides the necessary combination of properties required to serve as a support for the organic electrode materials (to the best of our knowledge, this is the first study of a 3D conductive support with an ordered submicron-porous structure being used in organic anodes). Polyimide-based nanoparticles (PIN) of multi-carbonyl polymers with low solubility to electrolytes and high theoretical capacity (1460 mAh g^{-1})[9,21] are employed as organic electroactive materials. The hybrid anode, consisting of the 3D Ni scaffold coated with a PIN layer (3D PIN/Ni) enables fast electrochemical reaction kinetics by providing efficient pathways for electrons and ions within the anode, as well as pathways for rapid ion transport provided by the continuous path of liquid electrolyte within the porous network. On the basis of the foregoing principal benefits, we realize efficient super-lithiation of 3D PIN/Ni which gives a high reversible capacity of 1260 mAh g^{-1} with 82.8% capacity retention over 250 cycles at 10C. Rates up to 400C for lithium-ion storage of organic anode are achieved for the first time and full anode-basis capacity (664 mAh g^{-1}/2810 mAh cm^{-3}) surpasses the target line required to meet the energy targets (1000 Wh kg^{-1}/1500 Wh L^{-1} on half-cell level) for fast-charge hybrid electric vehicles. We provide a deeper understanding of the reaction chemistry and underlying science of superior charge transfer through kinetics analysis of the 3D PIN/Ni. Our 3D periodic nano-network anode opens up intriguing possibilities for expediting the practical use of organic materials to realize fast and sustainable energy storage.

Results and discussion

Fabrication and characterization of a 3D bicontinuous nano-network electrode

Fig. 1a schematically outlines the fabrication process of 3D PIN/Ni. To construct the periodically arranged nanostructure of 3D PIN/Ni, we used a well-defined templating method via PnP.[15,16,19,20] The periodically porous 3D Ni support was formed by nickel electrodeposition through the optically patterned 3D epoxy template (periodicities in the XY-plane and Z-directions are 600 nm and 1.0 µm, respectively) (Fig. S1, ESI†).[14,22] After the template removal, the precursor solutions of mellitic acid and m-phenylenediamine were infiltrated into the sub-micron pores of the 3D Ni, followed by hydrothermal treatment at 180 °C for 3 h to induce a polycondensation reaction (Fig. S2, ESI†). The suggested unit molecular structure of the synthesized PIN,[9,21] comprising multi-ring carbonyl groups is shown in Fig. 1b. The mass loading of the redox-active PIN coated throughout the 3D Ni was controlled by varying the concentration of the precursor solutions (Fig. S3, ESI†). Structural characterization (Fig. 1c and Fig. S4, ESI†) shows the uniformity of the fabricated free-standing 3D PIN/Ni film (6.30 µm-thick) and that the PIN (radius of nanoparticles <100 nm) are conformally grown on the 3D Ni without clogging the pores (Fig. S5, ESI†). Fig. 1d depicts the scheme for energy storage in a half-cell containing the 3D PIN/Ni. This 3D architecture is expected to provide highly conductive electron pathways and short ion diffusion lengths. The periodically porous structure is further expected to be significantly advantageous in the formation of a uniform solid electrolyte interface (SEI) film that renders reversibility of redox reactions for stable long-term cycling. Furthermore, the interconnected open pore-network (average radius <300 nm in the XY-plane direction) ensures rapid ion transport within the electrolyte (Fig. S6, ESI†). The chemical composition of the as-fabricated 3D PIN/Ni identified by X-ray photoelectron spectroscopy (XPS) (Fig. S7, ESI†).[22] The XPS data confirms the successful formation of the PIN layer on the 3D Ni, being consistent with the proposed molecular structure of the PIN in Fig. 1b.

Verification of lithium storage capability

We evaluated the energy storage capability of the 3D PIN/Ni as electrodes in the LIB. Fig. 1e compares the initial galvanostatic lithiation/delithiation profiles of the 3D PIN/Ni (PIN/Ni = 52/48 (w/w)) and the conventional PIN anode (PIN/Super P/PTFE = 40/40/20 (w/w/w)) at 0.5C (750 mA g^{-1}). The specific

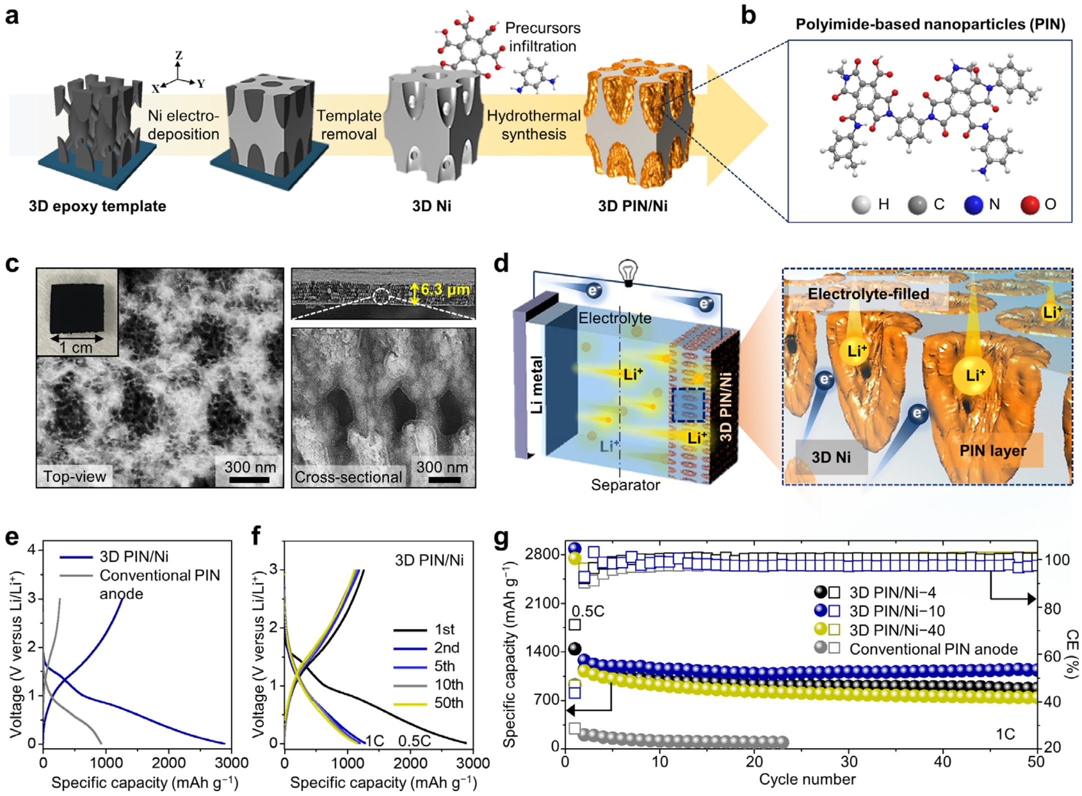

Fig. 1 Fabrication of the 3D bicontinuous nanostructured PIN/Ni electrode and its electrochemical performance. (a) Schematic illustrating the 3D PIN/Ni fabrication process. (b) Unit molecular structure of the redox-active PIN. (c) SEM images of the 3D PIN/Ni (inset: Digital image of the 3D PIN/Ni film). (d) Schematic of energy storage and electron/ion transport phenomena in a LIB containing the 3D PIN/Ni electrode. (e) Initial galvanostatic lithiation/delithiation profiles of the 3D PIN/Ni and the conventional PIN anode for the first electrochemical cycle within a voltage range of 0.01−3 V at 0.5C rate. (f) Galvanostatic lithiation/delithiation profiles of the 3D PIN/Ni over 50 cycles. (g) Cycling performance and Coulombic efficiency (CE) of the 3D PIN/Ni anodes with different active mass loading and the conventional PIN anode.

lithiation/delithiation capacities reach the high values of 2880/1260 mAh g^{-1} for the 3D PIN/Ni, whereas they were 925/266 mAh g^{-1} for the conventional PIN anode. We attribute such high specific capacities of the 3D PIN/Ni to the full-utilization of active materials at the first cycle and the facilitation of reaction kinetics through the bicontinuous pathways for electrons and ions. To gain a deeper understanding into the charge transfer kinetics in the internal structure of each electrode, the electrochemical impedance spectroscopy (EIS) profiles at the fully charged state are recorded (Fig. S8a and b, ESI†). In the high-medium frequency region, the 3D PIN/Ni shows a much smaller charge-transfer resistance (R_{ct}) value (71.9 Ω) than that of the conventional anode (559 Ω) (Table S1, ESI†), verifying the higher electronic/ionic conductivity, which is ascribed to the well-constructed nano-network structure. Furthermore, relationships between Z′ and $\omega^{-1/2}$ ($\omega = 2\pi f$) in the Warburg region of low-frequency are plotted to determine the Warburg factor (σ) (Fig. S8c, ESI†).[23] It is noteworthy that the σ value is related to the ion diffusion ability inside the electrode. The Li^+ diffusion coefficient of 3D PIN/Ni obtained from the σ value is calculated to be 42.9-fold higher than that of the conventional anode, which is mainly attributed to the short solid-state diffusion length within the nano-sized (i.e., low-dimension) PIN layer. Meanwhile, the 3D PIN/Ni and the conventional anode all show high irreversible capacities at the first cycle, giving rise to the low initial Coulombic efficiency (CE) of 43.7% and 28.8%, respectively. The low first-cycle CE is admittedly observed in organic anodes and can be ascribed to the growth of the SEI layer.[8–11] After a subsequent 5 cycles, the CE quickly saturates and remains over 97.5%, implying stable energy storage through reversible redox reactions of active PIN (Fig. 1f). To further underscore the effect of the regular arrangement of pores in the 3D PIN/Ni, a random porous Ni foam coated with PIN layer (PIN/Ni foam) was prepared (Fig. S9 and S10, ESI†). The electrochemical performance was scrutinized for the random porous PIN/Ni foam (Fig. S11 and S12, ESI†). The results clearly manifest that the higher reversible capacity and stable cyclability of the 3D PIN/Ni are originated not only from the 3D nanostructure but also from the electrolyte-filled network with regularly arranged pores.

We further examined the effect of the active mass loading on the cycle stability of 3D PIN/Ni (Fig. 1g). We term our nano-network anodes prepared with 4, 10, and 40 mg mL^{-1} of precursor solutions 3D PIN/Ni-4, 3D PIN/Ni-10, and 3D PIN/Ni-40, respectively. As shown in Fig. 1g, the 3D PIN/Ni-10 exhibits the highest capacity and stable cycling performance over 50 charge–discharge cycles. We believe that the two most likely reasons for the stable cyclability are i) the low solubility of polymer to the electrolyte and ii) the 3D periodic structure which enables nearly full-utilization of active materials as well as good electrolyte accessibility. We note that apparent capacity deterioration observed in the 3D PIN/Ni-40 appears to be due to the decreased porosity and the growth of microparticle impurities on the top surface (Fig. S13 and S14, ESI†). The high-resolution transmission electron microscopy (HR-TEM) images further support the highest specific capacity and superiority in cycling performance of 3D PIN/Ni-10 among the three anodes (Fig. S15, ESI†). The TEM image of the 3D PIN/Ni-10 (mass loading = 51.7 wt%) reveals that the few-layered PIN particles are homogeneously formed on the periodic 3D Ni, providing a large surface for electrochemical reactions and high lithium-ion accessibility, as well as good electrical contact with the conductive Ni scaffold. In comparison, the low density of the PIN particles (mass loading = 24.1 wt%) in the 3D PIN/Ni-4 leads to the limited formation of the SEI layer, contributing to the smallest irreversible capacity, which will be discussed more in detail later.[24] Furthermore, it is worth emphasizing that our 3D periodic nano-network design enables high loading density and areal capacity by effectively alleviating fatal issues of sluggish charge transfer kinetics and easy mechanical degradation in thick electrodes.[7] The maximum areal capacity of 5.99 mAh cm^{-2} is achieved by the 19.0 µm-thick 3D PIN/Ni-10 with an areal mass loading of 6.07 mg cm^{-2} (Fig. S16, ESI†).

Understanding the reaction mechanism

To thoroughly explore the redox behaviors and the reaction chemistry of the 3D PIN/Ni, we further analyzed the multiple spectroscopic data. According to the ex-situ XPS results of the 3D PIN/Ni at different depth of discharge (DOD) and state of charge (SOC) in the first cycle (as denoted in Fig. 2a), the redox-active PIN molecules show significant structural change during the first discharging and charging (Fig. 2b–d and Table S2, ESI†). At open-circuit voltage (OCV) state (point A), no Li 1s signal was detected and the intensity of the peak gradually increased during the lithiation of the 3D PIN/Ni. In the first step (A→B), one hydrogen atom in the carboxylic acid (COOH) group is irreversibly replaced by one lithium-ion, which is confirmed by new peaks of the carboxylic acid lithium salt (COOLi) group at 288.4 and 531.3 eV in the C 1s and O 1s spectra, respectively. Previously, it is reported that the carbonyl groups in the imide and amide are lithiated first because of the higher affinity to lithium ions than that of benzenes.[8,9] After the initial transformation from COOH to COOLi, all carbonyl groups in the 3D PIN/Ni undergo rapid and reversible lithiation followed by super-lithiation of unsaturated C=C bonds in conjugated

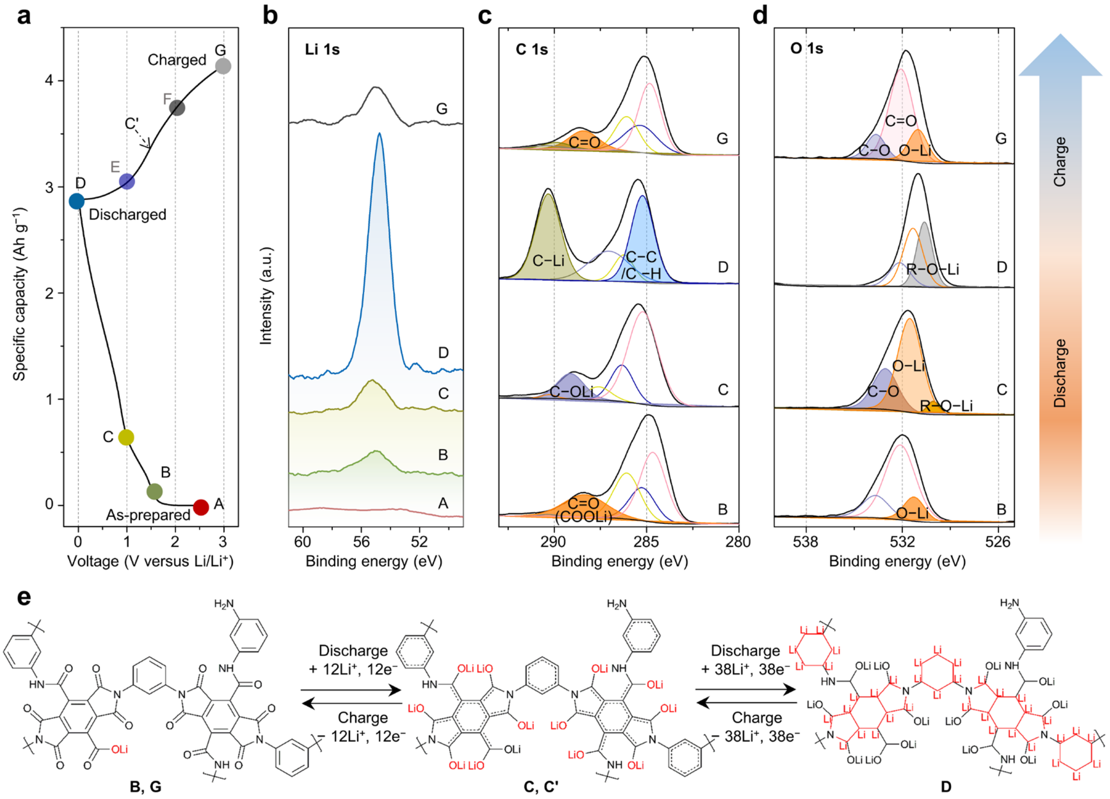

Fig. 2 Structural evolution investigated by XPS analysis and reaction mechanism. (a) Voltage profile of the 3D PIN/Ni during the first discharging and charging. XPS spectra of (b) Li 1s, (c) C 1s, and (d) O 1s region at the different electrochemical states corresponding to the selected points in (a). (e) The proposed reaction mechanism for lithium-ion storage.

aromatic benzene rings and imide rings, which is in good agreement with the XPS results and the previous findings.[8,9,25] It can be seen the O 1s peak with a binding energy of 531.5 eV corresponding to the O–Li bond significantly enhanced at the C stage, suggesting complete disappearance of C=O bonds in the second lithiation process (B→C). With the following discharging step (C→D), a pronounced peak at 290.3 eV for C–Li emerged[10] and the Li 1s signal is remarkably intensified, reflecting the super-lithiation with the acceptance of 38 lithium ions per repeating unit structure as proposed in Fig. 2e. We suspect that the efficient super-lithiation phenomenon on the 3D PIN/Ni is attributed to the nano-sized PIN active materials that are uniformly coated on the highly conductive Ni surface and form multiple ion transport channels. As fifty electrons in total per unit structure are capable of being involved in the reversible electrochemical reactions, the maximum theoretical capacity is calculated to be 1460 mAh g^{-1}, consistent with the obtained reversible capacities in Fig. 1g. During the delithiation process (D→C′→G), the C=C and C=O signals reappear, implying those active sites provide reversible lithium storage, while the Li 1s peak is still discerned at the fully delithiated G state, further verifying COOLi cannot be reversibly returned to COOH. The structural evolution of 3D PIN/Ni investigated by the Fourier-transform infrared (FT-IR) analysis supports the XPS results and further extends the spectroscopic understanding of the lithium storage proposed above (Fig. S17, ESI†).

Electrochemistry at different states of charge/discharge

The cyclic voltammetry (CV) and EIS results of the 3D PIN/Ni are assessed in Fig. 3. We showed the CV curves for the initial ten cycles in the 0.01–3 V range at a scan rate of 0.1 mV s^{-1} (Fig. 3b and c), which is in accordance with the expected lithium storage mechanism and the charge–discharge profiles. During the first cathodic process, there are two distinct broad peaks located at 1.5 and 0.80 V, which both become weaker within 5 cycles, clearly indicating the existence of the irreversible electrochemical process. Considering that the plateau around 0.80 V contributes most of the irreversible capacity in the initial charge–discharge curves in Fig. 3a, the peak at 0.80 V is partially ascribed to the SEI formation, while the other peak at 1.5 V can be explained by the overlapping of peaks for the irreversible transformation from COOH end group to COOLi, and the C=O lithiation. After five cycles, the redox couples of reduction/oxidation peaks centered at 1.5/1.5 V originating from the reversible reactions of C=O bonds, and the pairs at 0.93/0.81 V associated with the super-lithiation/delithiation of C=C bonds are observed. The redox pairs remain stable afterward and the CV curves almost overlap in the following cycles, demonstrating good electrochemical stability and reversibility of the 3D PIN/Ni.

We present the Nyquist plots of the 3D PIN/Ni at different electrochemical states denoted as points in Fig. 3a (Fig. 3d–f). As the electrode is discharged to 0.01 V (point B to D), the

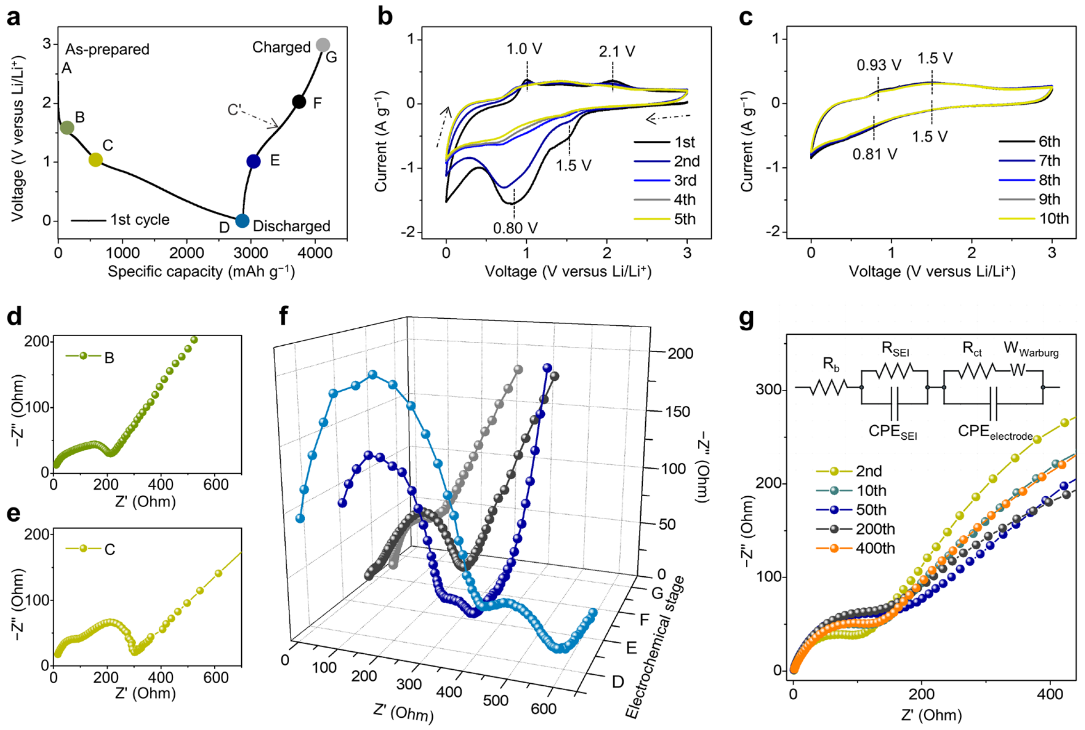

Fig. 3 Electrochemical changes in CV curves and Nyquist plots during lithiation/delithiation processes. (a) Voltage profile of the 3D PIN/Ni during the first cycle. CV curves of the 3D PIN/Ni in the 0.01–3 V range (b) from initial five cycles and (c) from 6th to 10th cycles. (d–f) The Nyquist plots of the 3D PIN/Ni at the different electrochemical states corresponding to the selected points in (a). (g) Impedance change with cycle number.

distinction of two parts in the non-symmetrical semicircular becomes clear: the first part in the higher frequency region is assigned to the resistance of SEI film (R_{SEI}), while the second part refers to the R_{ct}. The R_{SEI} value reaches 426 Ω at the fully-lithiated state (D), which is significantly larger than the values in the previous lithiation process (62.2 and 89.3 Ω at B and C, respectively) (Table S3, ESI†). Afterward, during the charging process to 3 V (point D to G), the overall impedance gradually decreases. To clarify why the 3D PIN/Ni-4 exhibits an unprecedentedly high first-cycle CE (72.5%) in Fig. 1g, we further compared the Nyquist plots of the 3D PIN/Ni-4 and -10 in the C and D states where the SEI film is mostly formed (Fig. S18, ESI†). As expected, the 3D PIN/Ni-4 shows lower R_{SEI} values of 53.2 and 152 Ω at the C and D states, respectively, validating that the low irreversible capacity of the 3D PIN/Ni-4 at the first cycle may be attributed to the limited SEI formation (Table S4, ESI†). However, if the SEI formation is too limited, the cyclability may suffer.[24] The formation of a stable protective SEI layer that inhibits side reactions with the electrolyte is of crucial importance to ensure stable cycle performance. Therefore, it leads us to believe the uniform and effective SEI layers were formed on the 3D PIN/Ni-10, correlating with the good cycle stability in Fig. 1g. The EIS profiles of 3D PIN/Ni at the fully charged state (G) with different electrochemical cycles are displayed in Fig. 3g. Due to the gradual formation of the SEI layer over the initial few cycles (Fig. S19, ESI†), the impedance slightly increases after 10 cycles. As the electrode is fully activated, the impedance starts to decrease after the 50th cycle, and the impedance barely changes even after 400 cycles, verifying the stabilized, uniform SEI layer formed on the 3D structure and the stability during cycling.

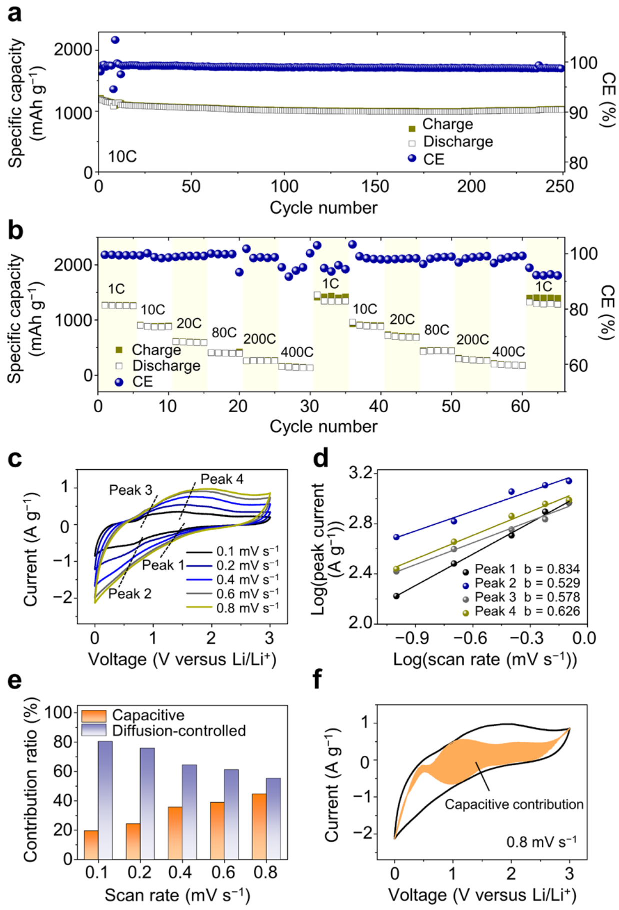

Fig. 4 High-rate cycling performance and kinetic characteristics. (a) Long-term cycling performance and CE over 250 cycles at 10C rate. (b) Capacity and CE at varying C-rates. The 3D PIN/Ni electrode was pre-cycled 50 times at 1C for activation before starting the measurements. (c) CV curves collected at different sweep rates for the 3D PIN/Ni electrode. (d) Peak current versus scan rate derived from (c) at the anodic and cathodic peaks. (e) Normalized contribution ratio of the capacitive (k_1v) and diffusion-controlled ($k_2v^{1/2}$) capacities at different sweep rates. (f) CV profile at a sweep rate of 0.8 mV s^{-1}. The shaded region (orange) of the CV corresponds to the capacitive current contribution.

High-performance rechargeable lithium organic batteries

A key advantage of our periodic nano-network structure of the 3D PIN/Ni is its high-rate cycling performance which is greatly challenging to achieve, especially in electrically insulating organic electrodes. Remarkably, the 3D PIN/Ni after activation process demonstrated stable capacity retention (>82.8%) and high CE (>98.7%) over 250 cycles at a high current density of 10C (Fig. 4a). Post-mortem analysis of the cycled cell (Fig. S20, ESI†) shows the nano-network anode retained its periodic structure, confirming the 3D Ni scaffold functions as a mechanical support as well as provides the continuous electron pathways. The rate capability of the 3D PIN/Ni was evaluated from 1C to 400C (600 A g^{-1}) as shown in Fig. 4b. Even at an ultrahigh rate of 400C, the 3D PIN/Ni delivered 13.8% (189 mAh g^{-1}) of its 1C capacity. The capacity recovered to 1300 mAh g^{-1} when the current density is returned to the 1C rate.

We elucidate the origin of the ultrahigh-rate capability in more detail through kinetic analysis based on CV measurements (Fig. 4c–f). The CV curves measured at various sweep rates from 0.1 to 0.8 mV s^{-1} are displayed in Fig. 4c. As the peak current (i) at the certain scan rate (v) follows the power law: $i = av^b$, the b values which reflect the lithium storage behaviors can be calculated from the plots of log(i) versus log(v) (Fig. 4d).[26] From the fitted line, high b values of 0.834 and 0.626 were obtained for the redox peak pair for C=O group-based reactions (peak 1 and 4), which demonstrates the considerable pseudocapacitive contribution. In contrast, b values bearing on the redox reactions of the conjugated carbon rings are 0.529 and 0.578 for peak 2 and peak 3, respectively. This is in line with the previous reports on polyimide with fast kinetics and the relatively slow diffusion-controlled kinetics of super-lithiation.[12,27] Although solid-state lithium-ion diffusion is a rate-limiting step at the higher rates, the 3D PIN/Ni still delivers 66.2% (904 mAh g^{-1}) of the 1C capacity at 10C as shown in Fig. 4a, due to the promoted super-lithiation through our 3D nanostructured electrode. It is scientifically meaningful to quantify the capacitive and diffusion-controlled contributions to understand the origin of the high capacity at the high scan rate.[28] We found that the normalized capacitive contribution ratio of the 3D PIN/Ni achieved from the calculated kinetic parameters gradually increases as the sweep rate increases (Fig. 4e and Fig. S21, ESI†). Specifically, 44.6% of the overall capacity at the scan rate of 0.8 mV s^{-1} is found to come from the capacitive contribution (Fig. 4f). Given the contribution results from the synergistic effect of fast capacitive reaction of polyimide and diffusion-controlled behavior in super-lithiation which gives high capacity, one could conclude the excellent rate capability reasonable.

The outstanding rate performance of our nano-network anode is highlighted by displaying the specific capacity of previously reported high-rate organic anodes as a function of the current rate. As plotted in Fig. 5a, the rate capability of the 3D PIN/Ni is superior to those of other organic anodes,[8–11,25,29–32] corroborating the strength of the proposed concept which utilizes the synergistic effect of the nano-sized active materials and the periodic nano-network architecture for rapid ion/electron pathways (Table S5, ESI†). We extended the comparison to include the high-performance inorganic-based anode materials (Fig. S22 and Table S6, ESI†).[33–37] Although the 3D Ni support is heavy, the 3D PIN/Ni does not require any additional conductive additive, binder, or metallic current collector, thereby the calculated capacity based on the total weight of the anode components of our anode is comparable to that of the high-performance inorganic anodes. It is worth noting that the full anode-basis capacity of the 3D PIN/Ni reaches 664 mAh g^{-1} (volumetric capacity of 2810 mAh cm^{-3}), suggesting its great potential as a future alternative to the traditional inorganic anodes.

Finally, in Fig. 5b, these specific and volumetric capacities of the 3D PIN/Ni are evaluated against the calculated capacity values required to fulfill the energy density targets (1000 Wh kg^{-1}/1500 Wh L^{-1} on half-cell level) of fast-charge advanced batteries for hybrid electric vehicles. The four target lines (marked as dashed lines in Fig. 5b) which correspond to virtual cells using the representative classes of cathode materials (e.g., conversion, layered intercalation, high-voltage spinel cathodes, and p-type organic cathodes) are derived as a function of the average anode potential in the half-cell (for detailed discussion, see supplementary text, ESI†). For the matching cathodes apart from the intercalation cathode (e.g., FeF_3) with the lowest average potential of 2.0 V versus Li/Li^+, the 3D PIN/Ni surpasses the challenging energy target values, demonstrating exceptionally high volumetric capacity. Only lithium, silicon, and germanium are above the specific capacity target line for the intercalation cathode. Further optimization through i) the molecular design of attaching an electron-donating group for lowering the anode potential and ii) the design of 3D conductive support that is lighter than the 3D Ni (e.g., a thin nanoshell structure) for higher gravimetric capacity would reduce this performance gap with the inorganic anodes and widen the choice of suitable cathodes.

Conclusions

In conclusion, we have demonstrated the lithographic fabrication of 3D periodic polyimide nano-networks for sustainable and fast lithium-ion storage. The 3D porous Ni support integrated with nano-sized multi-carbonyl polyimide provides continuous pathways for electrons and showed the 42.9-fold higher Li^+ diffusion coefficient than that of the conventional anode through the short solid-state diffusion length. Consequently, by promoting efficient super-lithiation in our 3D polyimide nano-network anode, the high specific capacity of 1260 mAh g^{-1} was realized and the cell retained 82.8% of the initial discharge capacity after 250 cycles, even at the high rate of 10C. The underlying mechanisms of ultrahigh-

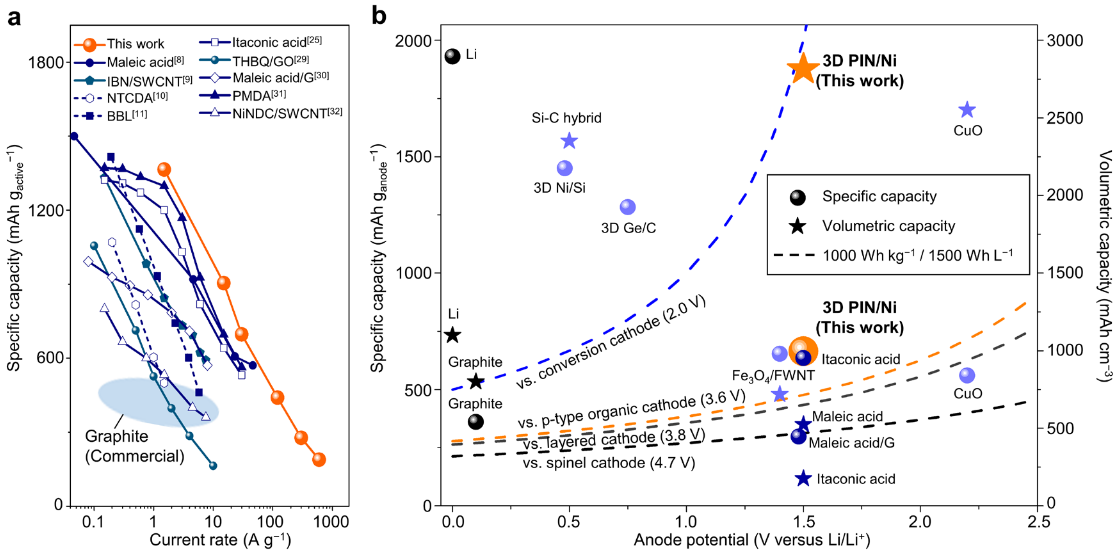

Fig. 5 Performance comparison of the 3D PIN/Ni with commercial and organic-based anodes. (a) Rate capability of the 3D PIN/Ni and other reported organic-based anodes toward lithium-ion storage. (b) Specific (sphere symbols) and volumetric capacities (star symbols) of anode materials as a function of the average anode potential. The specific capacities (expressed as mAh g_{anode}^{-1}) were estimated by considering the total mass of anode components. Dashed lines stand for the energy targets for each matching cathode.

rate capability (achieved rates up to 400C), which is the most important outcome in this work, were further identified by the spectroscopic understanding of the redox reaction chemistry and kinetic analysis of the dominating capacitive contribution in C=O reactions and diffusion-controlled behavior of super-lithiation. Furthermore, the PnP-based fabrication method described here enables control of pore size and porosity of the electrode structure through the phase mask design. We believe that deterministic control over the porosity of the 3D Ni scaffold could be further optimized for all-organic batteries to further improve the energy density. Nonetheless, it is worth noting that the 3D bicontinuous nano-network architecture in this study holds great significance as the general platform for high-performance organic electrodes, raising new feasibility for eco-friendly and promising energy storage.

Experimental section

Fabrication of the free-standing 3D Ni

A seed layer containing Ti (150 nm) was deposited on a SiO_2/Si wafer using an e-beam evaporator (SNTEK) for subsequent electrodeposition Ni. The Ti-deposited substrate was pretreated for 3 min by oxygen plasma. On the substrate, photopolymer films (SU-8, Microchem) with 10 and 20 μm thickness were spin-coated and soft-baked at 95 °C for 1 and 3 h, respectively. For the preparation of 3D epoxy template using PnP, the soft-baked films were exposed to a collimated Nd:YAG laser (355 nm, 300 mW, Advanced Optowave) through a conformal phase mask that has a surface relief grating of square arrays of pillar patterns (periodicity: 600 nm, relief depth: 400 nm). After the exposing and post-baking at 65 °C for 6 min, the films were placed in SU-8 developer (Microchem) to remove uncrosslinked areas. The fabricated epoxy templates were treated for 2 min by oxygen plasma, followed by the pulsed electrodeposition of Ni (2 mA cm^{-2}, 5 s on, 5 s off) for 4 and 12 h to prepare 6.3 and 19 μm-thick electrodes, respectively. Afterward, the samples were treated by microwave remote plasma source (STP compact, Muegge) to etch the epoxy template, forming the periodic 3D Ni in an inverted form. By chemical etching of Ti in a dilute hydrofluoric acid solution (10%, v/v), the free-standing 3D Ni films were stripped from the substrate.

Preparation of the 3D PIN/Ni electrode

The PIN particles were grown on the surface of the 3D Ni via the hydrothermal approach. Equal weights of mellitic acid and m-phenylenediamine were dissolved to prepare 4, 10, and 40 mg mL^{-1} aqueous solutions, respectively. The solution was poured into a Teflon-lined autoclave. The free-standing 3D Ni was soaked in ethanol and water to convert the surface to hydrophilic, then immersed in the precursor solution for 1 h. The autoclave was sealed, heated in a furnace at 180 °C for 3 h (heating rate: 1.3 °C min^{-1}). The fabricated 3D PIN/Ni was rinsed with water and ethanol, followed by drying at room temperature overnight.

Preparation of the conventional PIN electrode

The above hydrothermal synthesis was performed with 10 mg mL^{-1} precursor solution and the obtained powders were sequentially rinsed with water and ethanol using filter paper. After completely drying the powder under vacuum, the conventional PIN electrode was prepared by mixing 40% w/w active powders, 40% w/w Super P, and 20% w/w PTFE binder. The electrodes were free-standing films without current collectors.

Characterization

A field-emission scanning electron microscopy (SEM) (S4800, Hitachi) and TEM (Tecnai G2 F30, FEI company) at an accelerating voltage of 300 kV were used to analyze the structure and morphology of the 3D PIN/Ni. To explore the reaction mechanisms through spectroscopic analyses, we prepared the 3D PIN/Ni films at different electrochemical states by disassembling the coin cells (at different DOD and SOC in the first cycle) and rinsing the electrodes with ethylene carbonate in an Ar-filled glovebox. These samples were sealed to prevent air exposure. Afterward, all the samples were characterized by XPS (Sigma Probe, Thermo VG Scientific) and FT-IR (Nicolet iN10MX, Thermo Fisher Scientific). The mass loadings of PIN in the electrodes were estimated using a thermogravimetric analyzer (TG209 F1 Libra, NETZSCH).

Electrochemical measurements

The size of the 3D PIN/Ni and the conventional PIN electrodes were adjusted within the range of 0.30 ± 0.05 cm^2. In the Ar-filled glovebox, the electrodes were assembled into coin-type cells (CR2032) with polymer separators (Celgard 2400) and lithium metal. $LiPF_6$ (1 M) in ethylene carbonate and dimethyl carbonate (1:1, v/v) was utilized as an electrolyte. The coin cells were rested at room temperature for 24 h to promote the electrolyte wetting. The battery performance was evaluated using BCS cycler and VMP3 Potentiostat (Biologic) at various charge–discharge rates. The EIS measurements were conducted using a VersaSTAT3 system (AMETEK) over the frequency range of 10 kHz to 0.01 Hz.

Author Contributions

Y. H., S. J., and P. V. B. conceived the idea for the project. Y. H. performed the syntheses, material characterizations, and electrochemical measurements. N. F. and J. S. N. constructed settings for the battery cycler. N. F. and G. H. helped with the coin-cell fabrication and contributed to experimental design. Y. B. L. helped with the SEM and FT-IR analysis. Y. H. wrote the first draft. S. J., P. V.

B., and I.-D. K. commented on the manuscript. All authors discussed and analyzed the results.

Conflicts of interest

There are no conflicts to declare.

Acknowledgements

This research was supported by Creative Materials Discovery Program through the National Research Foundation of Korea (NRF), funded by the Ministry of Science, ICT, and Future Planning (2017M3D1A1039558). This work was also supported by Office of Naval Research (ONR) through the Defense University Research-to-Adoption (DURA) Initiative (N00014-18-S-F004).

References

1. B. Dunn, H. Kamath and J.-M. Tarascon, *Science*, 2011, **334**, 928−935.
2. D. Larcher and J.-M. Tarascon, *Nat. Chem.,* 2015, **7**, 19−29.
3. T. B. Schon, B. T. McAllister, P.-F. Li and D. S. Seferos, *Chem. Soc. Rev.*, 2016, **45**, 6345−6404.
4. Z. Song and H. Zhou, *Energy Environ. Sci.*, 2013, **6**, 2280−2301.
5. N. Oyama, T. Tatsuma, T. Sato and T. Sotomura, *Nature*, 1995, **373**, 598−600.
6. Y. Morita, S. Nishida, T. Murata, M. Moriguchi, A. Ueda, M. Satoh, K. Arifuku, K. Sato and T. Takui, *Nat. Mater.*, 2011, **10**, 947−951.
7. Y. Ham, V. Ri, J. Kim, Y. Yoon, J. Lee, K. Kang, K.-S. An, C. Kim and S. Jeon, *Nano Res.*, 2021, **14**, 1382−1389.
8. Y. Wang, Y. Deng, Q. Qu, X. Zheng, J. Zhang, G. Liu, V. S. Battaglia and H. Zheng, *ACS Energy Lett.*, 2017, **2**, 2140−2148.
9. J. Ryu, B. Park, J. Kang, D. Hong, S.-D. Kim, J.-K. Yoo, J. W. Yi, S. Park and Y. Oh, *ACS Nano*, 2019, **13**, 14357−14367.
10. Y. Xu, J. Chen, C. Ou, W. Lv, L. Tao and S. Zhong, *Nanoscale*, 2019, **11**, 15881−15891.
11. J. Wu, X. Rui, C. Wang, W. B. Pei, R. Lau, Q. Yan and Q. Zhang, *Adv. Energy Mater.*, 2015, **5**, 1402189.
12. S. v. Renault, V. A. Oltean, C. M. Araujo, A. Grigoriev, K. Edström and D. Brandell, *Chem. Mater.*, 2016, **28**, 1920−1926.
13. H. Yang, S. Liu, L. Cao, S. Jiang and H. Hou, *J. Mater. Chem. A*, 2018, **6**, 21216−21224.
14. S. K. Kuk, Y. Ham, K. Gopinath, P. Boonmongkolras, Y. Lee, Y. W. Lee, S. Kondaveeti, C. Ahn, B. Shin and J. K. Lee, *Adv. Energy Mater.*, 2019, **9**, 1900029.
15. S. Jeon, J.-U. Park, R. Cirelli, S. Yang, C. E. Heitzman, P. V. Braun, P. J. Kenis and J. A. Rogers, *Proc. Natl. Acad. Sci. U.S.A.*, 2004, **101**, 12428−12433.
16. C. Ahn, J. Park, D. Cho, G. Hyun, Y. Ham, K. Kim, S.-H. Nam, G. Bae, K. Lee and Y.-S. Shim, *Funct. Compos. Struct.*, 2019, **1**, 032002.
17. G. Hyun, J. T. Song, C. Ahn, Y. Ham, D. Cho, J. Oh and S. Jeon, *Proc. Natl. Acad. Sci. U.S.A.*, 2020, **117**, 5680−5685.
18. D. Cho, Y. S. Shim, J. W. Jung, S. H. Nam, S. Min, S. E. Lee, Y. Ham, K. Lee, J. Park and J. Shin, *Adv. Sci.*, 2020, **7**, 1903708.
19. J. K. Hyun, J. Park, E. Kim, L. J. Lauhon and S. Jeon, *Adv. Opt. Mater.*, 2014, **2**, 1213−1220.
20. J. Park, D. Tahk, C. Ahn, S. G. Im, S.-J. Choi, K.-Y. Suh and S. Jeon, *J. Mater. Chem. C*, 2014, **2**, 2316−2322.
21. T. Kim, B. Park, K. M. Lee, S. H. Joo, M. S. Kang, W. C. Yoo, S. K. Kwak and B.-S. Kim, *ACS Macro Lett.*, 2018, **7**, 1480−1485.
22. S. Kim, C. Ahn, Y. Cho, G. Hyun, S. Jeon and J. H. Park, *Nano Energy*, 2018, **54**, 184−191.
23. C. Li, S. Dong, R. Tang, X. Ge, Z. Zhang, C. Wang, Y. Lu and L. Yin, *Energy Environ. Sci.*, 2018, **11**, 3201−3211.
24. F. Zhang, G. Zhu, K. Wang, X. Qian, Y. Zhao, W. Luo and J. Yang, *J. Mater. Chem. A*, 2019, **7**, 17426−17434.
25. Y. Wang, W. Liu, R. Guo, Q. Qu, H. Zheng, J. Zhang and Y. Huang, *J. Mater. Chem. A*, 2019, **7**, 22621−22630.
26. V. Augustyn, J. Come, M. A. Lowe, J. W. Kim, P.-L. Taberna, S. H. Tolbert, H. D. Abruña, P. Simon and B. Dunn, *Nat. Mater.*, 2013, **12**, 518−522.
27. T. H. Le, Y. Yang, L. Yu, T. Gao, Z. Huang and F. Kang, *J. Appl. Polym. Sci.*, 2016, **133**.
28. S. Zheng, H. Huang, Y. Dong, S. Wang, F. Zhou, J. Qin, C. Sun, Y. Yu, Z.-S. Wu and X. Bao, *Energy Environ. Sci.*, 2020, **13**, 821−829.
29. Y. Wang, X. Li, L. Chen, Z. Xiong, J. Feng, L. Zhao, Z. Wang and Y. Zhao, *Carbon*, 2019, **155**, 445−452.
30. Y. Wang, X. Zheng, Q. Qu, G. Liu, V. S. Battglia and H. Zheng, *Carbon*, 2018, **132**, 420−429.
31. R. Guo, Y. Wang, S. Heng, G. Zhu, V. S. Battaglia and H. Zheng, *J. Power Sources*, 2019, **436**, 226848.
32. S.-H. Kim, H. H. Lee, J.-M. Kim, S. Y. Hong and S.-Y. Lee, *Energy Storage Mater.*, 2019, **19**, 130−136.
33. D. T. Ngo, H. T. Le, C. Kim, J.-Y. Lee, J. G. Fisher, I.-D. Kim and C.-J. Park, *Energy Environ. Sci.*, 2015, **8**, 3577−3588.
34. X. Zhang, D. Wang, X. Qiu, Y. Ma, D. Kong, K. Müllen, X. Li and L. Zhi, *Nat. Commun.*, 2020, **11**, 1−9.
35. Y. Liang, L. Chen, L. Cai, H. Liu, R. Fu, M. Zhang and D. Wu, *Chem. Commun.*, 2016, **52**, 803−806.
36. Y. H. Kwon, J. J. Park, L. M. Housel, K. Minnici, G. Zhang, S. R. Lee, S. W. Lee, Z. Chen, S. Noda and E. S. Takeuchi, *ACS Nano*, 2018, **12**, 3126−3139.
37. H. Zhang and P. V. Braun, *Nano Lett.*, 2012, **12**, 2778−2783.